Effect of site disorder on the asymptotic critical behaviour of $Ni_{75}Al_{25}$

Anita Semwal and S N Kaul[1]

School of Physics, University of Hyderabad, Central University PO, Hyderabad-500 046, Andhra Pradesh, India

E-mail: kaulsp@uohyd.ernet.in

Abstract
Extensive bulk magnetization and ac susceptibility measurements have been performed over a wide temperature range on well characterized polycrystalline $Ni_{75}Al_{25}$ samples 'prepared' in different states of site disorder. A detailed data analysis unambiguously establishes (i) the existence of multiplicative logarithmic corrections to the *mean-field* (MF) power laws in the asymptotic critical region near the ferromagnetic–paramagnetic phase transition and (ii) a gradual crossover to the *Gaussian* fixed point at temperatures outside the critical regime, *irrespective* of the degree of site disorder present. The latter crossover is followed by yet another crossover from Gaussian to pure MF regime in all the samples. Accurate determination of the universal amplitude ratio $R_\chi = DB^{\delta-1}\Gamma$, the asymptotic critical exponents β, γ and δ and the logarithmic correction exponents x^-, x^+ and x^0 for spontaneous magnetization, initial susceptibility and the magnetization versus field isotherm at the Curie temperature T_C, coupled with the observations made on the same system previously, not only rules out completely the possibility of isotropic short-range Heisenberg or isotropic long-range dipolar or uniaxial dipolar critical behaviour in $Ni_{75}Al_{25}$ but also indicates strongly that, in the asymptotic critical region, the weak itinerant-electron ferromagnet $Ni_{75}Al_{25}$ behaves as an *isotropic $d = 3$, $n = 3$* ferromagnet in which the attractive interactions between magnetic moments decay with intermoment distance (r) as $J(r) \sim 1/r^{(3/2)d}$, and that site disorder is *irrelevant* in the renormalization group sense.

1. Introduction

In *insulating* magnetic systems with spins *localized* at the lattice sites and interacting with one another through *short-range* (Heisenberg) exchange interactions, critical behaviour

is *solely governed* by the space (lattice) dimensionality d and order parameter (spin) dimensionality n. By contrast, in *metallic* magnets, the type and range of interactions coupling the 'atomic' magnetic moments essentially determine their properties in the critical region. Renormalization group (RG) calculations [1] on a homogeneous *isotropic d*-dimensional spin system with n-component order parameter and *long-range* attractive interactions between spins decaying with interspin distance, r, as $J(r) \sim r^{-(d+\sigma)}$ predict

 (i) mean-field (MF) (Gaussian) critical behaviour for all n when $\sigma < d/2$,
 (ii) MF critical behaviour with *logarithmic* corrections when $\sigma = d/2$,
(iii) a *new* fixed point, which is characterized by critical exponents that *depend on σ*, when $(d/2) < \sigma < 2$, and
(iv) short-range critical behaviour (i.e. the universality class primarily decided by the values of d and n) for *all d* when $\sigma > 2$.

While experiments on crystalline itinerant-electron ferromagnets Fe and Ni [2, 3] as well as Fe- and Co-based metallic glasses [4–7] have respectively confirmed predictions (iii) and (iv), there are strong indications that the perfectly *ordered* intermetallic compound Ni_3Al (a weak itinerant-electron ferromagnet) may be an experimental realization [8] of the theoretical result (iii). Thus, a study of critical phenomena in *band* magnets provides a powerful tool to probe the nature of interactions coupling the magnetic moments in such systems.

Heuristic arguments due to Harris [9] and RG calculations [10–12], based on the random-exchange Heisenberg (*short-range*) model (which includes both quenched random site- and bond-diluted Heisenberg models), assert that the addition of short-range frozen (quenched) disorder to a pure (ordered) spin system, which undergoes a second-order phase transition at a temperature T_C (Curie point), *does not affect* the sharpness and other critical properties of the transition if the specific heat critical exponent of the pure system, α_p, is *negative* (this result is better known as the Harris criterion). The Harris criterion is vindicated by the results of critical phenomenon investigations on a number of spin systems with quenched disorder [4–7, 13–16]. The influence of random disorder, which is invariably present in any real metallic alloy system, on the critical behaviour near the ferromagnetic–paramagnetic phase transition in band magnets with long-range interactions has not yet been theoretically addressed. Even from the experimental point of view, no consensus exists about the role of atomic (site or bond) disorder in affecting the critical behaviour of metallic ferromagnets. Conflicting reports [17–22] on the dependence of the critical exponents on the degree of disorder present in a given weak itinerant-electron ferromagnet and a large scatter in the values of the critical exponents have rendered the results of previous investigations inconclusive.

This situation prompted us to undertake a detailed systematic experimental study of the effect of site disorder on the magnetic properties in the critical region near the ferromagnetic–paramagnetic phase transition in a *well known* weak itinerant-electron ferromagnet, Ni_3Al. The rationale behind the choice of this system for the type of study intended is the following. $Ni_{75}Al_{25}$ undergoes (atomic) order–disorder phase transition at $\simeq 1450\,°C$ and hence the degree of site disorder in this alloy system can be altered in a *controlled* fashion through an appropriate choice and sequence of heat treatments. The *ordered* Ni_3Al compound thus forms a well characterized (*reference*) system [8] for a study which intends to clearly bring out the influence of the site disorder on the critical behaviour.

2. Sample preparation and characterization

2.1. Preparation

Ultra-high-purity (99.999%) nickel and aluminium taken in stoichiometric proportions by weight were melted together in a recrystallized alumina crucible under high-purity (99.999%)

argon gas inert atmosphere by a radio frequency (RF) induction technique. The $Ni_{75}Al_{25}$ alloy, in a completely molten state, was kept in the crucible for a couple of minutes for homogenization and then poured into a cylindrical hole in a massive copper mould. The entire operation from melting to pouring was carried out under argon pressure of >1 atm. Polycrystalline $Ni_{75}Al_{25}$ was thus prepared in the form of a rod, 10 mm in diameter and 100 mm in length. Spheres of 3 mm diameter, rectangular parallelopipeds of dimensions $40 \times 2.5 \times 0.5$ mm^3 and discs of 10 mm diameter and 5 mm thickness were spark-cut from the rod. One each of the spheres, rectangular parallelopipeds and discs was annealed at 520 °C for 16 d in quartz tubes evacuated to a pressure of 10^{-7} Torr and subsequently water-quenched. A portion of the 'as-prepared' polycrystalline rod was *melt-quenched* (ejected at a temperature of 1500 °C and helium pressure of 200 mbar) on to a rotating copper wheel to form long thin ribbons of width 2 mm and thickness $\sim$30 μm. Yet another $Ni_{75}Al_{25}$ ingot prepared by the RF induction method was re-molten and an attempt was made to grow a single crystal by the Bridgman technique. However, this attempt was not successful in that a highly strained polycrystalline sample of cylindrical shape was formed. A sphere of 2.5 mm diameter and a disc of 10 mm diameter and 5 mm thickness was spark-cut from this cylindrical sample. The samples in the 'highly strained', 'annealed' and 'quenched' states are henceforth referred to as S_1, S_2 and S_3, respectively.

2.2. Characterization

With a view to confirming that the samples indeed conform to the stoichiometric composition $Ni_{75}Al_{25}$, the pieces remaining after spark-cutting samples S_1, S_2 and S_3 were analysed for chemical composition using the x-ray fluorescence technique and inductively coupled plasma-optical emission spectroscopy. The actual chemical composition of these samples is given in table 1. Extensive x-ray diffraction measurements, using Cu Kα radiation, have been performed on disc-shaped samples at room temperature over the angle, 2θ, range of $10° \leqslant 2\theta \leqslant 100°$. The observed x-ray patterns, shown in figure 1, could be completely indexed on the basis of the $L1_2$ cubic structure and the refined values of the lattice parameter, displayed in table 1, have been obtained employing the well known Nelson–Riley–Taylor–Sinclair method [23]. Drastically reduced peak intensity and considerably large widths of the Bragg peaks in sample S_1 are the manifestation of a high level of internal strain and compositional inhomogeneity. In the case of the quenched sample S_3, *satellite* (*s*) peaks of *lower* intensity accompany the *main* (*m*) Bragg peaks of *higher* intensity and occur at *higher* Bragg angles, θ_B, (figure 1). Moreover, the satellite peaks are *uniformly* (systematically) shifted with respect to the main peaks, i.e. $\theta_B^s - \theta_B^m \equiv \phi = 0.29(1)°$. The splitting of the main as well as satellite (220) peaks into K$_{\alpha_1}$ and K$_{\alpha_2}$ components is also clearly noticed from the x-ray pattern shown in figure 1. The occurrence of satellite peaks signals the existence of two interpenetrating face-centred-cubic (fcc) lattices of different interplanar spacings d_m and d_s corresponding to the main and satellite reflections. The interplanar spacings d_m and d_s are related through the expression $(1/d_s) = (1/d_m) + \phi\sqrt{(2/\lambda)^2 - (1/d_m)^2}$ or, alternatively, by $d_s = d_m/(1 + \phi \cot \theta_B^m)$, where λ is the wavelength of the incident x-ray radiation. The interatomic spacings for the two interpenetrating fcc lattices that give rise to main and satellite reflections, respectively, turn out to be $a_m = 3.5650(10)$ Å and $a_s = 3.5619(5)$ Å. Another important finding is that the quenched sample S_3 has a strong (200) texture. By contrast, the annealed sample S_2 exhibits no such texture, sharper Bragg peaks (figure 1) and thus a much higher degree of site order, as expected.

From the observed *integrated* intensities I_S and I_F of the Cu_3Au-type (100) or (110) superstructure (*S*) and the fcc type (200) or (220) fundamental (*F*) Bragg reflection peaks
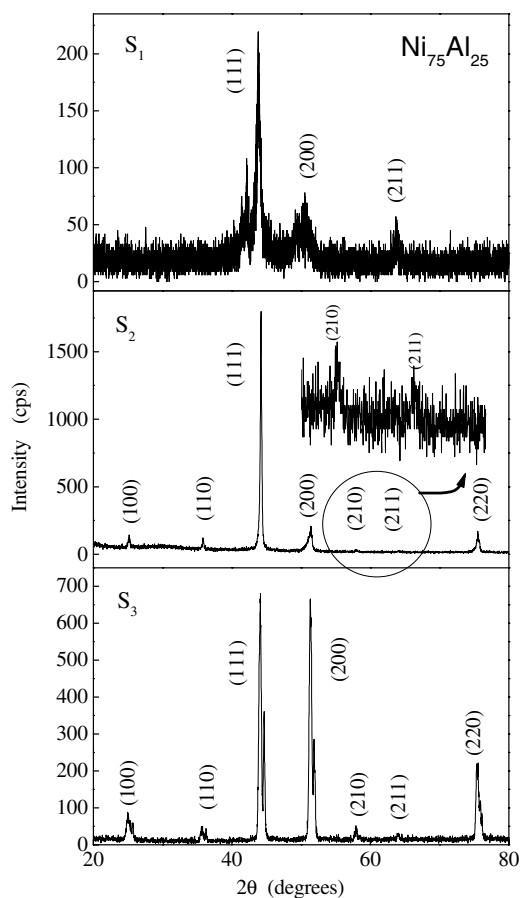
Figure 1. X-ray diffraction patterns for the Ni$_3$Al samples S$_1$, S$_2$ and S$_3$ in the angle range (2θ) 20°–80°. The enlarged view of (210) and (211) peaks for S$_2$ (encircled region) is also shown in the figure.

Table 1. Nominal and actual composition, lattice parameter (a) and LRO parameter.

Sample	Nominal composition		Actual composition		a (Å)	LRO parameter ($\mathcal{S}$)
	Ni (at.%)	Al (at.%)	Ni (at.%)	Al (at.%)		
S$_1$	75.00	25.00	74.73(13)	25.20(19)	3.5686(14)	0.77(4)
S$_2$	75.00	25.00	75.08(17)	25.21(10)	3.5650(15)	0.95(2)
S$_3$	75.00	25.00	75.08(17)	25.21(10)	3.5650(10)[a]	0.76(4)
					3.5619(5)[a]	

[a] Values corresponding to two sub-lattices.

in a given sample, the long-range order (LRO) parameter, $\mathcal{S}$, has been estimated using the relation [24] $\mathcal{S}^2 = (I_S/I_F)_{sample}(I_F/I_S)_{\mathcal{S}=1}$, where $(I_F/I_S)_{\mathcal{S}=1}$ is the corresponding intensity ratio for the *fully ordered* Ni$_3$Al sample. In the absence of the experimental value of the ratio $(I_F/I_S)_{\mathcal{S}=1}$, this ratio is calculated from the expression

$$(I_F/I_S)_{\mathcal{S}=1} = \frac{[\{X_{Ni}f_{Ni}(\theta) + X_{Al}f_{Al}(\theta)\}_F^2\{L_P(\theta)\}_F\{\exp(-2M(\theta))_F\}]}{[\{f_{Ni}(\theta) - f_{Al}(\theta)\}_S^2\{L_P(\theta)\}_S\{\exp(-2M(\theta))_S\}]}, \quad (1)$$

where X_{Ni} and X_{Al} are the concentrations of Ni and Al atoms in atomic percent, f_{Ni} and f_{Al} are the atomic structure factors for Ni and Al, the Lorentz polarization factor $L_P = (1 + \cos^2 2\theta)/\sin^2\theta\cos\theta$, 2θ is the Bragg angle, $\exp(-2M)$ is the Debye–Waller factor with $M(\theta) = (3h^2/m_a k_B \Theta_D)\{(\phi(x)/x) + (1/4)\}(\sin^2\theta/\lambda^2)$, the Debye integral $\phi(x) = (1/x)\int_0^x \xi \, d\xi/(e^\xi - 1)$, the Debye temperature $= \Theta_D$, $x = \Theta_D/T$ and the mass of the atom $= m_a$. In equation (1), the subscripts F and S refer, respectively, to the fundamental and superstructure reflections. The values of f_{Ni}, f_{Al}, L_P and $\exp(-2M)$ corresponding to the angles at which (100), (200) or (110), (220) Bragg reflections occur [25] in the fully ordered Ni$_3$Al compound are taken from the standard international tables [26, 27] and inserted into equation (1) to obtain the theoretical estimates for the ratio $[I_F^{(200)}/I_S^{(100)}]_{\mathcal{S}=1}$ or $[I_F^{(220)}/I_S^{(110)}]_{\mathcal{S}=1}$. The LRO parameter is then calculated from the reflections $\mathcal{S}^2 = [I_S^{(100)}/I_F^{(200)}]_{meas} \times [I_F^{(200)}/I_S^{(100)}]_{\mathcal{S}=1}$ and/or $\mathcal{S}^2 = [I_S^{(110)}/I_F^{(220)}]_{meas} \times [I_F^{(220)}/I_S^{(110)}]_{\mathcal{S}=1}$, where the subscript *meas* denotes the measured integrated intensity ratio for a given sample. The values of $\mathcal{S}$, so obtained, are listed in table 1. The present value of the lattice parameter for the fully ordered Ni$_3$Al sample, S$_2$, conforms well with those reported [25, 28] previously. Note that the value $\mathcal{S} = 0.55(30)$ for sample S$_2$ quoted in [8, 29] is *wrong* because instead of the *integrated* intensity ratio, the *peak* intensity ratio [25] was used for $(I_F/I_S)_{\mathcal{S}=1}$ to calculate $\mathcal{S}$.

In the *ordered* Ni$_3$Al intermetallic compound, Ni and Al atoms respectively occupy face centres (A sites) and corners (B sites) of the fcc unit cell. In a partially ordered Ni$_{75}$Al$_{25}$ alloy, if the right (Ni on A, Al on B) and wrong (Ni on B, Al on A) atoms are denoted by r and w, the total number of atoms on the A or B sites is given by $n = r + w$. The LRO parameter, defined by $S = (r - w)/n = (2r/n) - 1$, is equal to unity for the completely ordered case when $r = n$. According to this definition, the observed values of S (table 1) indicate that 88.5 ± 2.0 (11.5 ± 2.0), 97.5 ± 1.0 (2.5 ± 1.0) and 88 ± 2 $(12 \pm 2)\%$ of A or B sites are occupied by Ni (Al) or Al (Ni) atoms in samples S$_1$, S$_2$ and S$_3$, respectively.

3. Experimental details

High-resolution (50 ppm) magnetization, $M(T, H_{ext})$, measurements were performed on well characterized *polycrystalline* samples S$_1$–S$_3$ of nominal composition Ni$_{75}$Al$_{25}$ in external static magnetic fields (H_{ext}) up to 15 kOe over a wide temperature range, 15 K $\leqslant T \leqslant$ 300 K, embracing the critical region near the ferromagnetic–paramagnetic phase transition. While samples S$_1$ and S$_2$ were spheres of diameters 2.5 and 3 mm, respectively, sample S$_3$ was in the form of a stacked bundle consisting of several alloy ribbon strips, each of 2.2 mm length and 2 mm width, stacked one above the other after a thin coat of Apeizon N grease had been applied in between them to ensure a good thermal contact between the ribbon strips. In order to minimize the demagnetizing effects, sample S$_3$ was rotated (after placing it in the sample holder assembly) such that H_{ext} lies within the ribbon plane and is directed along the length of the ribbons. Such an operation was not needed in the case of samples S$_1$ and S$_2$, where the demagnetizing factor does not depend on the direction of H_{ext}. Sample temperature was monitored by a pre-calibrated platinum sensor which is in body contact (hence in good thermal contact) with the sample, and kept constant to within ± 5 mK by a proportional integrator and derivative temperature controller. The demagnetizing factor, N, was computed from the inverse slope of the magnetization (M) versus H_{ext} straight-line (i.e. $4\pi N = (\text{slope})^{-1} = H_{ext}/M$) isotherm taken at the lowest temperature $T = 15$ K in the field range -20 Oe $\leqslant H_{ext} \leqslant$ 20 Oe. A rough estimate of the Curie temperature, T_C, was obtained
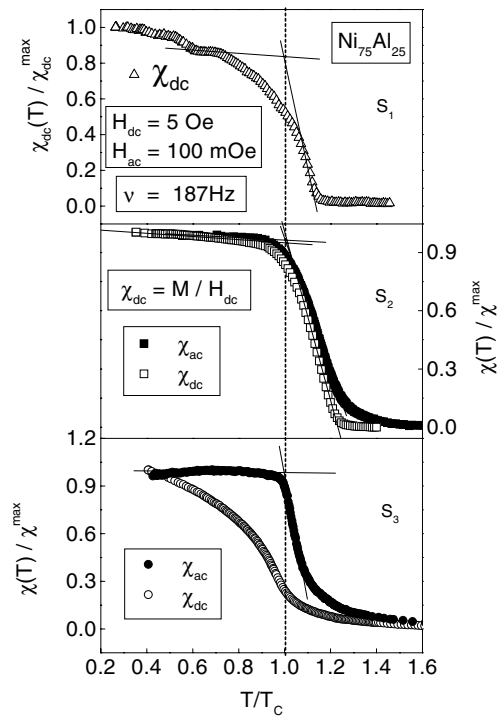
Figure 2. Temperature variations of ac susceptibility, χ_{ac} (closed symbols), measured at the rms driving ac field of magnitude 100 mOe and frequency 187 Hz, and dc susceptibility, χ_{dc} (open symbols), measured in an external dc field of 5 Oe; both $\chi_{ac}(T)$ and $\chi_{dc}(T)$ are normalized to their maximum values. The straight lines drawn through the data points illustrate the 'kink-point' determination of T_C as the temperature at which these straight lines intersect one another.

by identifying T_C with the temperature at which a '*knee*' occurs in the thermomagnetic curve taken at $H_{ext} = 5$ Oe in the field-cooled mode. Such curves for samples S_1–S_3 are depicted in figure 2. Magnetization versus external magnetic field isotherms were taken on all the three samples at 60 predetermined but fixed values (each stable to within ± 1 Oe) ranging from 0 to 15 kOe at temperature intervals of 0.5, 0.1, 0.05 and 0.025 K in the ranges 15 K $\leqslant T \leqslant 0.5T_C$, $0.5T_C \leqslant T \leqslant T_C - 10$ K, $T_C - 10$ K $\leqslant T \leqslant T_C - 3$ K and $T_C - 3$ K $\leqslant T \leqslant T_C + 3$ K, respectively. Above $T_C + 3$ K, the temperature interval was slowly increased to 0.1, 0.5, 1, 5 and 10 K until room temperature was reached.

After compensating for the earth's magnetic field, the 'in-phase' component of ac susceptibility (χ_{ac}) was measured to a relative accuracy of ~ 10 ppm on several rectangular strips each of dimensions $40 \times 2.5 \times 0.5 \, (0.03)$ mm^3 of samples S_1, S_2 (S_3) at various *fixed* rms amplitudes (1 mOe $\leqslant H_{ac} \leqslant 100$ mOe) and frequencies (18.7 Hz $\leqslant \nu \leqslant 187$ Hz) of the ac driving field H_{ac} (applied along the length in the sample plane) in the temperature interval 10 K $\leqslant T \leqslant 120$ K. Considerations such as the optimum signal-to-noise ratio and *linear* response to H_{ac} at a given temperature restrict the choice of H_{ac} and ν to 10 mOe and 87 Hz, respectively. The demagnetizing factor N was extracted from the relation $\chi^{-1}(T) = \chi_{ac}^{-1}(T) - 4\pi N$ using N as a parameter such that at $T = T_C$, $\chi_{ac}^{-1}(T_C) = 4\pi N$ as $\chi^{-1}(T_C) = 0$. The values of N so determined ($N = 0.006$ and 0.0004 for samples S_2 and S_3) and those deduced from the low-field magnetization versus H_{ext} isotherms agree quite well with those calculated from the well known Osborn formula using the actual sample dimensions.

Figure 2 compares the dc susceptibility (measured at $H_{ext} \equiv H_{dc} = 5$ Oe), *normalized* to its maximum value, $[\chi_{dc}(T)/\chi_{dc}^{max}]_{H_{ext}=5\ Oe}$, plotted against the reduced temperature, T/T_C, for samples S_2 and S_3 with the corresponding *normalized* ac susceptibility (taken at $H_{ac} = 100$ mOe and $\nu = 187$ Hz), $\chi_{ac}(T)/\chi_{ac}^{max}$, versus T/T_C plots. This figure also displays the $[\chi_{dc}(T)/\chi_{dc}^{max}]_{H_{ext}=5\ Oe}$ versus T/T_C plot for sample S_1. Note that the values of T_C for samples S_1–S_3, determined by an elaborate critical-point analysis (to be described later), have been used to construct these plots. Based on the well known relation $(1/M_{meas}) = (1/M_{int}) + [1/(H_{ext}/4\pi N)]$ between the *measured* magnetization (M_{meas}) and *internal* or 'zero-field' magnetization (M_{int}) for a ferromagnet at low fields, two cases need to be distinguished.

Case 1. When $H_{ext} \ll 4\pi N$, $M_{meas} \simeq H_{ext}/4\pi N$ or $\chi_{meas} = M_{meas}/H_{ext} = (4\pi N)^{-1}$; i.e. at such low fields, the measured susceptibility is *demagnetization-limited* for temperatures below T_C.

Case 2. When $H_{ext} \gg 4\pi N$, $M_{meas}(T) \simeq M_{int}(T)$; i.e., the measured magnetization essentially follows the temperature dependence of spontaneous magnetization for $T \leqslant T_C$.

$\chi_{dc}(T)$ or equivalently, $M_{meas}(T)$ at $H_{ext} = 5$ Oe for sample S_3 ($\chi_{ac}(T)$ for samples S_2 and S_3, and $\chi_{dc}(T)$ for samples S_1 and S_2) corresponds (correspond) to case 2 (case 1). Other important observations include the following:

(i) with increasing field, the temperature, T_K (at which the 'knee' in $\chi(T)$ occurs) shifts to lower temperatures and $\chi(T)$ is more sensitive to field in the *quenched* sample S_3 than in the *annealed* sample S_2, and

(ii) $\chi_{dc}(T)$ exhibits more than one *plateau* for $T < T_C$ in sample S_1, indicating thereby that the sample is chemically *inhomogeneous* and contains magnetic phases of different Curie temperatures.

The latter inference is consistent with that drawn from the x-ray data shown in figure 1.

4. Results and discussion

After correcting the external magnetic field for demagnetization (i.e. $H = H_{ext} - 4\pi N M(T, H_{ext})$), the raw $M - H_{ext}$ isotherms taken in the critical region are used to construct the $[M(T, H)]^{1/\beta}$ versus $[H/M(T, H)]^{1/\gamma}$ plots, better known as the modified Arrott plots (MAPs), with the *choice* of the critical exponents β and γ for spontaneous magnetization and initial susceptibility ($\beta = 0.5$ and $\gamma = 1.0$ in the present case, figure 3) that makes the MAP isotherms for temperatures close to T_C *linear* [6, 7, 13, 16] over the widest possible H/M range. The origin of the pronounced concave downward (upward) curvature (figure 3) in the MAP isotherms at low fields for $T \ll T_C$ ($T \gg T_C$), inherent to ferromagnetic systems, has been discussed at length in [13]. Moreover, the MF values of the exponents β and γ (indicating that the critical fluctuations of the order parameter are not as important as they normally are for $d = 3$ spin systems) as well as a very low value of magnetization even at 4.2 K in the present case ensure that the MF magnetic equation of state is valid over unusually wide ranges of T and H. The 'zero-field' quantities such as spontaneous magnetization, $M(T, 0)$, and inverse initial susceptibility, $\chi^{-1}(T) \equiv \chi_{dc}^{-1}(T)$, are computed from the intercept values at different temperatures on the ordinate ($T \lesssim T_C$) and abscissa ($T \gtrsim T_C$) obtained when the *linear* high-field portions of the $[M(T, H)]^2$ versus $[H/M(T, H)]$ (Arrott plot (AP)) isotherms are extrapolated to $H = 0$ and $M^2 = 0$, respectively, as illustrated by the typical APs shown in figure 3. For sample S_1 the AP isotherms develop a slight concave upward curvature as the temperature is raised through the Curie temperature. Such a departure from linearity basically
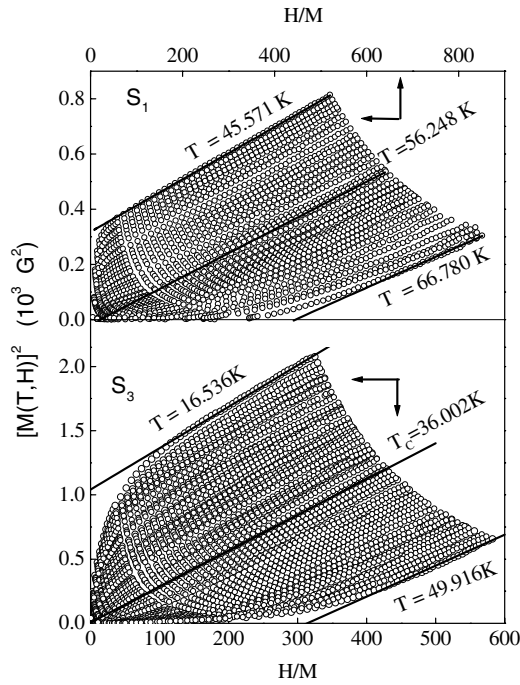
Figure 3. MAPs, i.e. $M^{1/\beta}$ versus $(H/M)^{1/\gamma}$ plots with $\beta = 0.5$ and $\gamma = 1.0$, for Ni$_3$Al over a wide temperature range around T_C for samples S$_1$ and S$_3$.

reflects the presence of more than one magnetic phase in this sample; ferromagnetic phase with higher (lower) T_C constitutes the majority (minority) phase. APs yield Curie temperature as the temperature at which the M^2–(H/M) isotherm is *linear* over nearly the entire H/M range (down to the lowest value of H/M for samples S$_2$ and S$_3$, and for $(H/M) > 240$ for S$_1$) and upon extrapolation passes through the origin. With T_C, $M(T, 0)$ and $\chi^{-1}(T)$ determined in this way from the AP, spontaneous magnetization and inverse initial susceptibility are plotted against reduced temperature, $\epsilon = (T - T_C)/T_C$, in figures 4 and 5 over a wide temperature range that includes the critical region. The relation $\chi(T) = \chi_{ac}(T)/[1 - 4\pi N \chi_{ac}(T)]$ asserts that $\chi_{ac}(T)$ is a direct measure of the 'zero-field' intrinsic susceptibility, $\chi(T)$. Henceforth, $\chi(T)$ data obtained through extrapolation and those measured directly at $H_{ac} = 10$ mOe and $\nu = 87$ Hz are referred to as $\chi_{dc}(T)$ and $\chi_{ac}(T)$, respectively.

With a view to ascertaining the true asymptotic critical behaviour of the weak itinerant ferromagnets in question and to bringing out clearly the role of site disorder, the $M(T, 0)$, $\chi(T)$ and $M(T_C, H)$ data are analysed employing a method whose details are given elsewhere [8] and which makes use of the expressions that exhaust all the possibilities from the theoretical standpoint [1, 29–31] by either including or excluding the leading *multiplicative* logarithmic correction (MLC) or *additive* logarithmic correction (ALC), non-analytic correction (NAC) to the single power laws (SPLs).

Using the expressions

$$M(T, 0) = B_{eff}(-\epsilon)^{\beta_{eff}} \qquad \epsilon < 0 \qquad\qquad (2)$$

$$\chi^{-1}(T) = \Gamma_{eff}^{-1}\epsilon^{\gamma_{eff}} \qquad \epsilon > 0 \qquad\qquad (3)$$

the *effective* critical exponents β_{eff} and γ_{eff}, defined as $\beta_{eff}(\epsilon) = d[\ln M(|\epsilon|)]/d(\ln |\epsilon|)$ and $\gamma_{eff}(\epsilon) = d[\ln \chi^{-1}(\epsilon)]/d(\ln \epsilon)$, are calculated at different temperatures from the $M(\epsilon)$
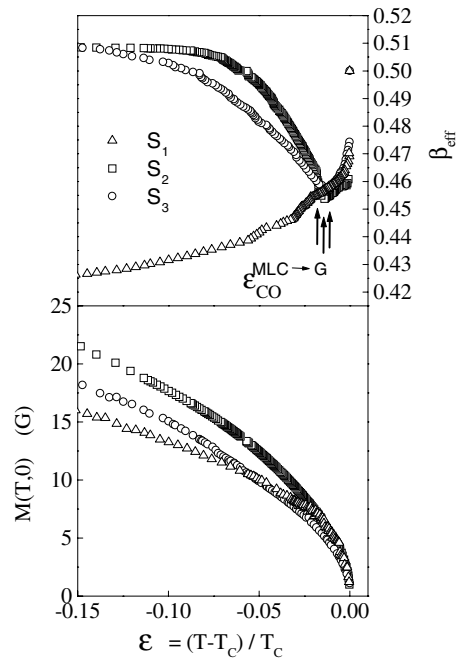
Figure 4. Temperature variations of the spontaneous magnetization, $M(T, 0)$, and its effective critical exponent, β_{eff}. The upward arrows indicate the reduced temperatures, $\epsilon_{CO}^{MLC \to G}$, that mark the onset of a crossover from asymptotic critical behaviour to the Gaussian regime.
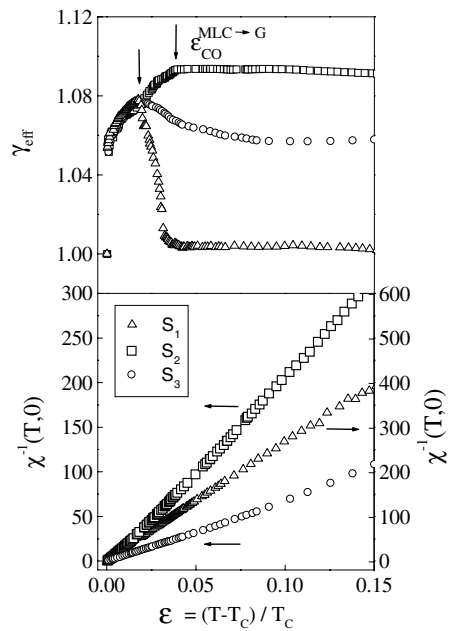
Figure 5. Temperature variations of the inverse initial (dc) susceptibility, $\chi^{-1}(T) \equiv \chi_{dc}^{-1}(T)$, and its effective critical exponent, γ_{eff}. The downward arrows indicate the reduced temperatures, $\epsilon_{CO}^{MLC \to G}$, that mark the onset of a crossover from asymptotic critical behaviour to the Gaussian regime. The horizontal arrows indicate the ordinate scales for the $\chi^{-1}(T)$ data.

and $\chi^{-1}(\epsilon)$ data depicted in figures 4 and 5. $\beta_{eff}(\epsilon)$ and $\gamma_{eff}(\epsilon)$, so obtained, are also displayed in these figures. In the plots of β_{eff} versus ϵ (figure 4) and γ_{eff} versus ϵ (figure 5), $\epsilon_{CO}^{LC \to G}$ marks the temperature (indicated by arrows) at which a crossover from the asymptotic to non-asymptotic critical behaviour occurs. Thus the asymptotic critical region spans the temperature ranges for $M(T, 0)$ and $\chi_{dc}(T)$ displayed in table 2. An elaborate 'range-of-fit' analysis [3–8, 32] of the $M(T, 0)$, $\chi^{-1}(T)$ and $M(T_C, H)$ data (taken in the asymptotic critical region) reveals the following. (I) Neither the SPL, equations (2) and (3), nor the expressions involving either the ALC or the NAC but *only those*

$$M(T, 0) = B(-\epsilon)^{\beta} |\ln |\epsilon||^{x^-} \qquad \epsilon < 0 \qquad (4)$$

and

$$\chi^{-1}(T) = \Gamma^{-1} \epsilon^{\gamma} |\ln |\epsilon||^{-x^+} \qquad \epsilon > 0 \qquad (5)$$

that *include* the leading MLC reproduce the observed temperature variations of $M(T, 0)$ (figure 6) and $\chi_{ac}^{-1}(T)$ or $\chi_{dc}^{-1}(T)$ (figure 7) accurately. (II) By contrast, the MLC fit (depicted in figure 8 by the continuous curve) to the critical isotherm, $M(T_C, H)$, based on the expression

$$H = DM^{\delta} |\ln |M||^{-\delta x^0} \qquad \epsilon = 0, \qquad (6)$$

is *marginally better* than the SPL fit based on

$$H = D_{eff} M^{\delta_{eff}} \qquad \epsilon = 0 \qquad (7)$$

or even the ALC and NAC fits. (III) When the lower bound $|\epsilon_{min}|(M_{min})$ of the fit range is kept constant and the upper bound $|\epsilon_{max}|(M_{max})$ is varied in the 'range-of-fit' analysis, the parameters corresponding to the SPL/ALC/NAC fits vary *monotonously* while those associated with the MLC fits remain essentially *unaltered* (within the uncertainty limits) as $|\epsilon_{max}|(M_{max})$ increases. Note that the parameter variations with $|\epsilon_{max}|(M_{max})$ are the *same* for the SPL, ALC and NAC fits. Figures 7–9 in [8] serve to illustrate the above-mentioned parameter variations.

Observation (I) is vindicated by the robustness of the fitting parameters against variation in the range of fit and by the result that the percentage deviation of the $M(T, 0)$ and $\chi_{ac}^{-1}(T)$, $\chi_{dc}^{-1}(T)$ data from the best least-squares fits based on equations (4) and (5) is *smaller* in magnitude and *evenly* distributed around the theoretically calculated values, whereas the optimum SPL/ALC/NAC fits present *systematic* deviations from the data, so much so that such deviations blow up as $\epsilon \to 0$. By comparison, the percentage deviation of the $M(T_C, H)$ data from the optimum fits based on equations (6) and (7) does not permit a clear-cut distinction between the MLC and SPL fits to be made. However, a slightly lower (by nearly 8%) value of the sum of deviation squares and substantially lower deviations at low fields in the case of the MLC fit does tilt the balance in its favour. Figures 4–6 in [8] represent the typical deviation plots. The *optimum* MLC fits to the $M(T, 0)$, $\chi_{ac}^{-1}(T)$, $\chi_{dc}^{-1}(T)$ and $M(T_C, H)$ data are depicted by the *continuous curves* in figures 6–8. Based on the variations of the fitting parameters in the asymptotic critical region yielded by the 'range-of-fit' analysis [3–8, 32], we arrive at the final values for the quantities of interest listed in table 2. Note that all the independent determinations of the Curie temperature for a given sample (table 2) from the $M(T, 0)$, $\chi_{ac}^{-1}(T)$, $\chi_{dc}^{-1}(T)$ and $M(T_C, H)$ data yield the *same* value within the uncertainty limits, i.e. $T_C^- = T_C^0 = T_C^+$, as is demanded by the consistency between different data sets taken on the same sample. Moreover, χ_{ac} (direct method) and χ_{dc} (indirect method involving extrapolation to zero field) yield *identical* values (table 2) for the *universal* quantities such as the asymptotic critical exponents and MLC exponents. Figures 7–9 in [8] serve to illustrate this behaviour.
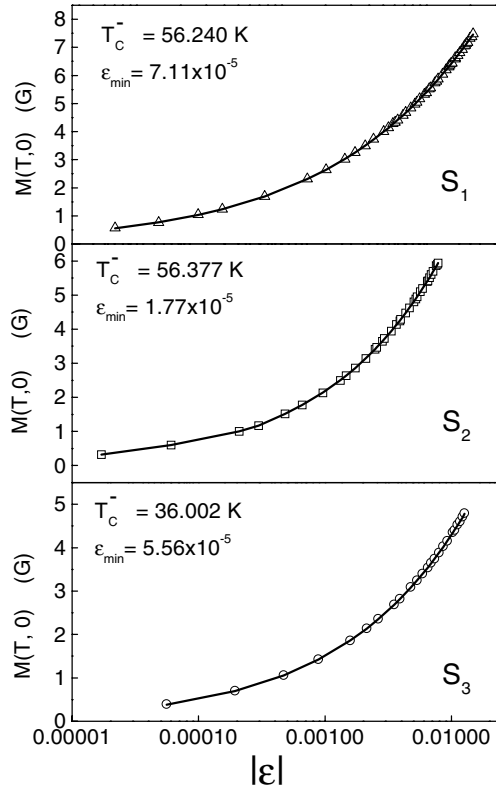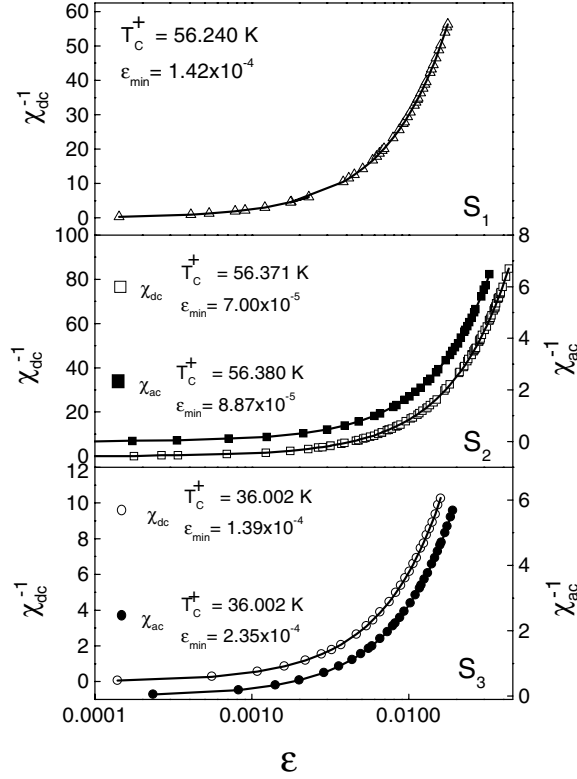
Figure 6. Spontaneous magnetization, $M(T, 0)$, as a function of reduced temperature. The continuous curves through the $M(T, 0)$ data (open symbols) are the optimum MLC fits based on equation (4).

While MF values of the asymptotic critical exponents β, γ and δ rule out the possibility of an isotropic Heisenberg or isotropic dipolar critical behaviour in Ni$_3$Al, the logarithmic corrections to MF power laws seem to suggest that Ni$_3$Al may belong to one of those universality classes for which the RG theories predict such corrections. These classes are

(a) systems with [33] spin dimensionality 'n' and space dimensionality $d = 4$,
(b) *uniaxial* dipolar ferromagnets [31] with $d = 3$ and $n = 1$,
(c) *isotropic d*-dimensional ferromagnets with n-component spins and attractive interactions between spins decaying with interspin distance, r, as [1] $J(r) \sim 1/r^{(3/2)d}$ and
(d) the same as (c) but with [34] $n \to \infty$ (spherical model).

Obviously, the universality classes (a) and (d) are not applicable to the three-dimensional ferromagnets in question. Logarithmic corrections to the MF power laws have previously been observed in a number of uniaxial dipolar ferromagnets (for details refer to the references cited in Frey *et al* [31] and [32]). In table 2, the experimental values of the critical exponents, the exponents x^-, x^+ and x^0 of the logarithmic correction terms, defined by the equations (4)–(6), as well as the universal amplitude ratio $R_\chi = DB^{\delta-1}\Gamma$, are compared with the corresponding theoretical estimates [1,31] predicted for the universality classes (b) and (c). Such a comparison between theory and experiment reveals that the values of x^-, x^+, x^0 and R_χ determined in this work are completely different from those predicted by theory for a $d = 3$ uniaxial dipolar

Figure 7. Inverse initial susceptibility, $\chi_{dc}^{-1}(T)$ or $\chi_{ac}^{-1}(T)$, as a function of reduced temperature. The continuous curves through the $\chi_{dc}^{-1}(T)$ (open symbols) or $\chi_{ac}^{-1}(T)$ (closed symbols) data are the optimum MLC fits based on equation (5).

ferromagnet. By contrast, the RG calculations for a $d = 3$, $n = 3$ isotropic ferromagnet in which the interaction between spins decays as $J(r) \sim 1/r^{(3/2)d}$ yield the estimates for the exponents x^- and x^+ that are in very good agreement with the experimental values. However, such an agreement should be treated with caution since no theoretical estimates for the quantities x^0 and R_χ are currently available. Another important point to note is that the critical exponents, universal amplitude ratio and exponents of the leading logarithmic correction have the *same* values (within the uncertainty limits) for all three samples S_1–S_3 (table 2). This observation asserts that site disorder has *no influence* on the asymptotic critical behaviour of the weak itinerant-electron ferromagnet, $Ni_{75}Al_{25}$.

The 'range-of-fit' analysis of $M(T, 0)$ and $\chi_{dc}^{-1}(T)$ data taken at temperatures outside the asymptotic critical region, based on equations (2)–(5), reveals the following magnetic behaviour in this temperature region. The optimum fits (continuous curves) to the $[M(T, 0)]^{1/\beta_{eff}}$ versus $(-\epsilon)$ and $[\chi^{-1}(T)]^{1/\gamma_{eff}}$ versus ϵ data, based on the expressions

$$M(T, 0) = B'(-\epsilon)^\beta [1 + a_M(-\epsilon)^{\Delta_M}] \qquad \epsilon < 0 \qquad (8)$$

$$\chi^{-1}(T) = \Gamma'^{-1}\epsilon^\gamma [1 + a_\chi\,\epsilon^{\Delta_\chi}]^{-1} \qquad \epsilon > 0 \qquad (9)$$

(which include the corrections to MF leading exponents arising from Gaussian fluctuations) with $\Delta_M = \Delta_\chi$ *fixed* at 1.0, as expected for the Gaussian (G) fixed point and the values for the parameters B', β and a_M in equation (8) and Γ'^{-1}, γ and a_χ in equation (9) displayed in
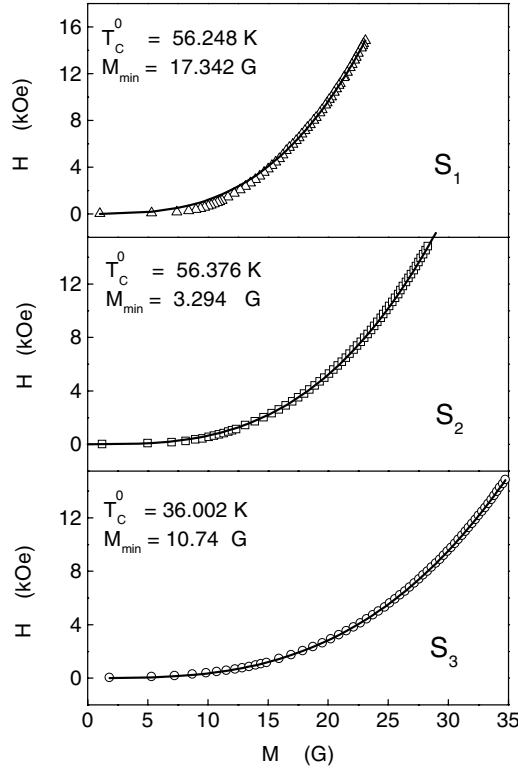
Figure 8. H versus M isotherms at $T = T_C$ for different samples. The continuous curves through the $H(M)$ data are the optimum MLC fits based on equation (6).

table 3, describe the data *better* than the pure MF power laws (dashed lines), i.e. equations (2) and (3) with $\beta_{eff} = 0.5$ and $\gamma_{eff} = 1.0$, in the temperature ranges specified in table 3, as is evident from figure 9. In order to highlight this observation, β_{eff} and γ_{eff} are plotted against the reduced temperature $\epsilon^G = (T - T_C^G)/T_C^G$ (referred to the Curie temperature T_C^G of the Gaussian (G) fixed point) for temperatures on either side of T_C^G in figure 10. The straight line fits through the $\beta_{eff}(\epsilon^G)$ and $\gamma_{eff}(\epsilon^G)$ data points are based on the expressions

$$\beta_{eff}(\epsilon^G) = \beta^G + a_M \Delta_M (-\epsilon^G)^{\Delta_M} \tag{10}$$

and

$$\gamma_{eff}(\epsilon^G) = \gamma^G + a_\chi \Delta_\chi (\epsilon^G)^{\Delta_\chi} \tag{11}$$

that relate the *effective* (β_{eff}, γ_{eff}) and *asymptotic* (β^G, γ^G) critical exponents, defined by equations (2), (3) and (8), (9), respectively, for the Gaussian fixed point. Note that $\beta^G = \lim_{\epsilon^G \to 0} \beta_{eff}(\epsilon^G)$ ($\gamma^G = \lim_{\epsilon^G \to 0} \gamma_{eff}(\epsilon^G)$) and if $\Delta_M = \Delta_\chi = 1$, β_{eff} versus ϵ^G and γ_{eff} versus ϵ^G plots are *straight lines* with slopes (intercepts on β_{eff} and γ_{eff} axes) a_M and a_χ (β^G and γ^G), respectively. That this is indeed the case in specific temperature ranges below and above T_C^G is demonstrated by the data presented in figure 10. The values of β^G, a_M, γ^G and a_χ deduced from the linear $\beta_{eff}(\epsilon^G)$ and $\gamma_{eff}(\epsilon^G)$ plots serve as a cross-check for those (table 3) obtained from the optimum fits (continuous curves in figure 9) to the $M(T, 0)$ and $\chi^{-1}(T)$ data, based on equations (8) and (9). Another important point to note is that if the Gaussian corrections were not important, β_{eff} and γ_{eff} would remain constant at the MF

Table 2. Comparison between experiment and theory.

		Experiment			Theory $d=3, n=3$ $J(r) \sim r^{-(3/2)d}$ [1]	Theory $d=3, n=1$ Uniaxial dipolar [31]
Parameters	Method	S_1	S_2	S_3		
Fit range $\epsilon(10^{-4})$		0.070–210	0.18–133	0.056–127		
T_C^- (K)	$M(T,0)$/LC	56.240(5)	56.377(5)	36.002(5)	—	—
B_{eff}	$M(T,0)$/SPL	44(3)	47(3)	38(2)	—	—
β_{eff}	$M(T,0)$/SPL	0.46(1)	0.48(2)	0.46(1)	—	—
B	$M(T,0)$/MLC	35.62(2)	34.9(2)	28.83(6)	—	—
β	$M(T,0)$/MLC	0.5000	0.501(1)	0.5000(3)	0.5	0.5
x^-	$M(T,0)$/MLC	0.2727(2)	0.2745(25)	0.2727(5)	3/11	1/3
Fit range $\epsilon(10^{-4})$	χ_{dc}	1.4–177	0.7–433	1.39–160		
	χ_{ac}		0.89–327	2.35–191		
T_C^+ (K)	χ_{dc}/MLC	56.240(5)	56.371(5)	36.002(5)	—	—
	χ_{ac}/MLC		56.380(5)	36.002(5)	—	—
Γ_{eff}^{-1}	χ_{dc}/SPL	3843(447)	2315(212)	777(170)	—	—
	χ_{ac}/SPL		262(17)	381(24)	—	—
γ_{eff}	χ_{dc}/SPL	1.065(13)	1.075(20)	1.065(3)	—	—
	χ_{ac}/SPL		1.092(12)	1.072(9)	—	—
Γ^{-1}	χ_{dc}/MLC	5997(5)	3300(20)	1210(20)	—	—
	χ_{ac}/MLC		345(1)	556.35(48)	—	—
γ	χ_{dc}/MLC	1.0000(2)	0.9992(15)	0.9993(8)	1.0	1.0
	χ_{ac}/MLC		0.9995(5)	1.0000(4)	1.0	1.0
x^+	χ_{dc}/MLC	0.4545(2)	0.4545(55)	0.4545(58)	5/11	1/3
	χ_{ac}/MLC		0.4546(5)	0.4545(20)		
Fit range M (G)		17.34–34.75	3.2–28.2	10.74–23.09		
T_C^0 (K)	$M(T_C,H)$/MLC	56.240(5)	56.376(5)	36.002(5)	—	—
D_{eff}	$M(T_C,H)$/SPL	1.2035(8)	0.654(4)	0.3550(17)	—	—
δ_{eff}	$M(T_C,H)$/SPL	2.9999(1)	2.9985(35)	2.993(10)	—	—
D	$M(T_C,H)$/MLC	1.2171(4)	0.651(4)	0.3585(20)	—	—
δ	$M(T_C,H)$/MLC	3.0000(1)	3.004(4)	3.0000(15)	3.0	3.0
x^0	$M(T_C,H)$/MLC	0.00333	0.0033(3)	0.0036(4)	—	1/3
R_χ		0.26(1)	0.25(1)	0.24(1)	—	0.5
$\beta+\gamma$		1.49997	1.501(2)	1.4993	1.5	1.5
$\beta\delta$		1.500(1)	1.505(5)	1.4999(3)	1.5	1.5

values $\beta = 0.5$ and $\gamma = 1.0$ within the temperature ranges in question. Finite slopes of the $\beta_{eff}(\epsilon^G)$ and $\gamma_{eff}(\epsilon^G)$ linear plots (figure 10), therefore, assert that the Gaussian corrections are significant. Furthermore, it is evident from the $\beta_{eff}(\epsilon)$ and $\gamma_{eff}(\epsilon)$ data shown in figures 4 and 5, as well as from the $\beta_{eff}(\epsilon^G)$, $\gamma_{eff}(\epsilon^G)$ plots (figure 10) that a crossover from the asymptotic critical behaviour, characterized by MLC to MF power laws, to the Gaussian (G) fixed point occurs gradually over a fairly wide temperature range; $\epsilon_{CO}^{MLC \to G}$ ($\epsilon_{CO}^{G \to MLC}$) and $\epsilon_{CO}^{G \to MF}$ mark the onset temperatures for the MLC $\to$ G (G $\to$ MLC) and G $\to$ MF crossovers with respect to $T_C^{MLC} \equiv T_C$ (T_C^G) and T_C^G, respectively.
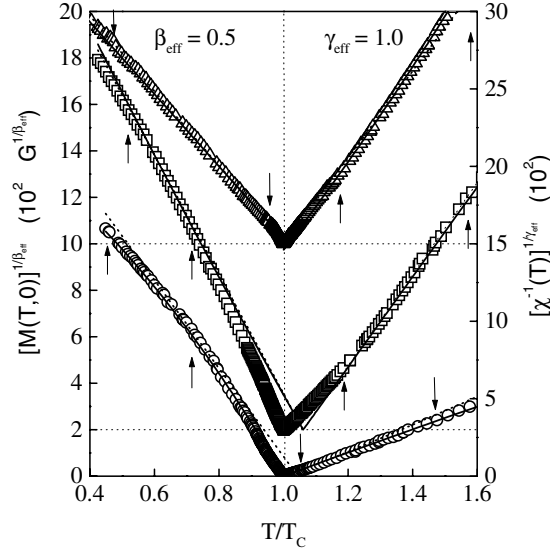
Figure 9. In order to highlight the importance of the corrections to the MF behaviour arising from Gaussian fluctuations, the quantities $[M(T, 0)]^{1/\beta_{eff}}$ and $[\chi^{-1}(T)]^{1/\gamma_{eff}}$ with the MF choice ($\beta_{eff} = 0.5$ and $\gamma_{eff} = 1.0$) of the exponents β_{eff} and γ_{eff} are plotted against temperature. The best least-squares MF and Gaussian fits to the data, based on equations (2), (3) and (8), (9) of the text, are depicted by the dashed straight lines and solid curves, respectively. If the Gaussian corrections are not important, such plots should be *linear* (dashed straight lines) over the temperature intervals marked by the upward or downward arrows below and above the Gaussian Curie temperature, T_C^G. For the sake of clarity, the origin (which should actually read as *zero*) of the ordinate scales for samples S$_1$ (open triangles) and S$_2$ (open squares) has been shifted up.

Table 3. Values of various parameters in the Gaussian and MF regimes. Numbers in the parentheses denote uncertainty in the least significant figure.

| Sample | Gaussian ϵ range | | β_G | γ_G | T_C^G (K) | a_M | a_χ | Curie–Weiss range (in ϵ) | q_C | q_S | q_C/q_S |
	$M(T, 0)$	$\chi^{-1}(T)$									
S$_1$	-0.55 to -0.29	0.16–0.58	0.495 (5)	1.002 (3)	57.04 (4)	0.025 (5)	0.085 (5)	1.20–2.77	0.375	0.0616	6.17 (3)
S$_2$	-0.44 to -0.34	0.18–0.58	0.500 (9)	0.995 (5)	59.8 (2)	-0.075 (5)	0.025 (2)	1.31–3.52	0.358	0.0575	6.23 (2)
S$_3$	-0.45 to -0.32	0.17–0.37	0.497 (3)	1.005 (5)	36.43 (3)	-0.19 (3)	0.011 (5)	—	—	0.0428	—

Taking cognizance of the fact that the symmetry of the Hamiltonian and/or range of interaction govern the asymptotic critical behaviour of metallic ferromagnets, an attempt is made to rationalize the present observation that the asymptotic critical behaviour of Ni$_{75}$A$_{25}$ is characterized by MF power laws with logarithmic corrections. To this end, the following observations merit serious consideration. A detailed investigation [35] of magnetocrystalline anisotropy on ordered Ni$_3$Al single crystals has revealed that the leading anisotropy constant *vanishes* as the Curie temperature is approached from below. In view of this finding, Ni$_3$Al is expected to behave as an *isotropic* spin system in the asymptotic critical region. Considering that the ratio of the spin-wave stiffness, D, to the Curie temperature, T_C, is a *direct* measure of
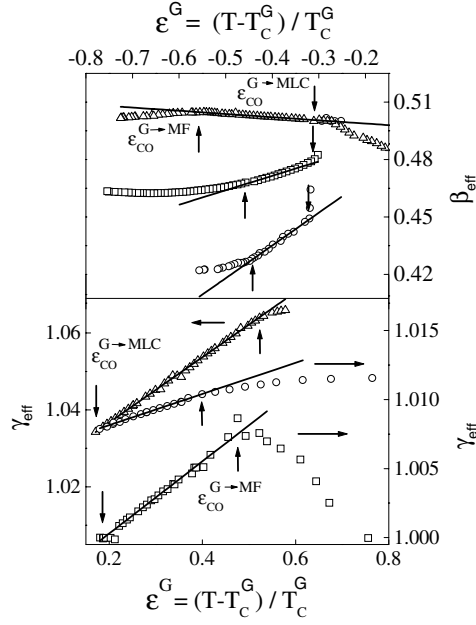
Figure 10. Effective critical exponents β_{eff} and γ_{eff} plotted against the reduced temperature, $\epsilon^G = (T - T_C^G)/T_C^G$, referred to the Gaussian fixed-point critical temperature T_C^G. The straight lines through the data points (open triangles, squares and circles for samples S_1, S_2 and S_3, respectively) represent the best least-squares fits based on equations (10) and (11) of the text. The downward and upward arrows indicate the reduced temperatures (*referred* to the Curie temperature T_C^G of the Gaussian fixed point) $\epsilon_{CO}^{G \to MLC}$ and $\epsilon_{CO}^{G \to MF}$ that mark the onset of Gaussian $\to$ the fixed point (characterized by MLC to MF power laws) and Gaussian $\to$ pure MF crossovers, respectively. The horizontal arrows indicate the relevant ordinate scale.

the range of interaction in the localized-electron model, the value $(D/T_C) \simeq 1.25$ meV Å^2 K^{-1} reported [29, 36, 37] previously for Ni$_{75}$Al$_{25}$ regardless of the degree of site disorder present, when compared with the estimate $(D/T_C) = 0.144$ meV Å^2 K^{-1} predicted [38] by the nearest-neighbour Heisenberg model, asserts that the interactions coupling the magnetic moments in Ni$_{75}$Al$_{25}$ are of *long-range* type. The $\chi^{-1}(T)$ data for samples S_1 and S_2, displayed in figure 11, follow the Curie–Weiss behaviour in the temperature ranges specified in table 3. By contrast, magnetic susceptibility of the quenched sample (S_3) does not obey the Curie–Weiss law even up to temperatures as high as $6T_C$, as is evident from figure 11. Persistence of the deviations from the Curie–Weiss behaviour and the curvature in the M versus H isotherms up to $T \simeq 6T_C$ indicates the presence of short-range magnetic order in this sample even at such high temperatures. It is only for temperatures in the vicinity of room temperature (300 K) that the Curie–Weiss behaviour is observed in S_3. The inverse slope of the straight-line fit, based on the Curie–Weiss law, yields the Curie constant, C, which, in turn, permits an accurate determination of the effective atomic moment in the paramagnetic state, q_C, through the relation $q_C(q_C + 2) = (2.828)^2 CA/\rho$, where A and ρ are the atomic weight and density, respectively. The values of q_C, so obtained, and the previously reported [29, 37] numerical estimates for the magnetic moment per alloy atom at 0 K, q_S, for the currently investigated samples are listed in table 3. The q_C/q_S ratio, which is also displayed in table 3, turns out to be very large compared with the value $(q_C/q_S) = 1.0$, which is the case when magnetic moments are *localized* at the lattice sites. According to the Rhodes–Wohlfarth criterion [39],
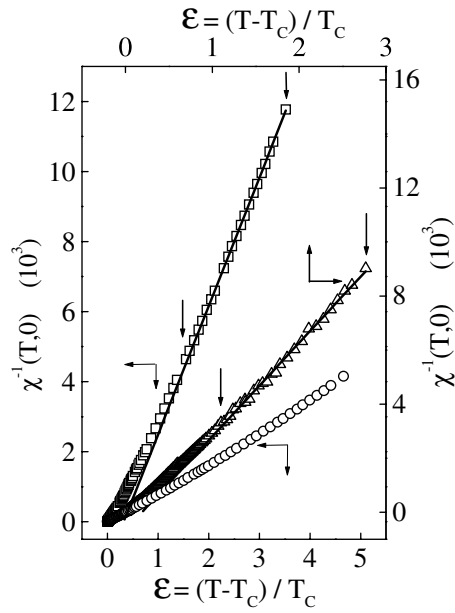
Figure 11. Inverse initial susceptibility, $\chi_{dc}^{-1} \equiv \chi^{-1}$, plotted against the reduced temperature, ϵ, over a wide temperature range above T_C. The solid lines indicate the Curie–Weiss fits to the data and the downward arrows mark the temperature range over which the Curie–Weiss law is valid.

the larger the value of the q_C/q_S ratio compared with unity, the more *itinerant* are the magnetic moments. Therefore, it follows that

(i) the localized moment picture cannot form a correct theoretical description of the magnetism in Ni$_{75}$Al$_{25}$ and

(ii) the long-range interactions such as the dipole–dipole and the Ruderman–Kittel–Kasuya–Yosida (RKKY) interactions are not relevant to the case under consideration.

Even otherwise, the dipole–dipole interactions, which are proportional to the magnetic moment *squared*, are expected to be extremely weak in Ni$_{75}$Al$_{25}$ due to the small magnitude of q_S (an order of magnitude smaller than in crystalline Ni).

Observation of logarithmic corrections to the MF power laws and a close agreement between the values $x^- = 0.2745(25)$ and $x^+ = 0.4545(55)$ and those ($x^- = 3/11$ and $x^+ = 5/11$) characterizing the asymptotic critical behaviour of an *isotropic $d = 3$, $n = 3$* ferromagnet in which interactions between spins decay [1] with the interspin distance (r) as $J(r) \sim 1/r^{(3/2)d}$ (table 2), when viewed in the light of the above remarks, rule out completely the possibilities such as (a) isotropic short-range Heisenberg, (b) isotropic long-range dipolar and (iii) uniaxial dipolar for the asymptotic critical behaviour of Ni$_{75}$Al$_{25}$. They do, however, indicate that the weak itinerant ferromagnet Ni$_{75}$Al$_{25}$ may be a *potential* candidate for the universality class for critical-point phenomena represented by the *marginal* case $d = 3$, $n = 3$ and $\sigma = d/2$ of the RG calculations [1] on an *isotropic* ferromagnet with space dimensionality d, spin dimensionality n and long-range attractive interactions between spins of the form $J(r) \sim 1/r^{d+\sigma}$. A cautious approach in interpreting the above-mentioned agreement between theory and experiment is warranted by the fact that the theoretical estimates for the universal amplitude ratio $R_\chi = DB^{\delta-1}\Gamma$ and the logarithmic correction exponent x^0 are not currently

available. However, based on the present work, the following *definite* conclusions can be drawn.

(i) The site disorder is *irrelevant* in the RG sense.
(ii) A series of crossovers, MF with logarithmic corrections $\rightarrow$ Gaussian $\rightarrow$ pure MF, occurs as the temperature increasingly deviates on either side of T_C.

Detailed RG calculations are needed to unravel the physics behind the above observations.

Acknowledgments

References

[1] Fisher M E, Ma S K and Nickel B G 1972 *Phys. Rev. Lett.* **29** 917
[2] Arajs A, Tehan B L, Anderson E E and Stelmach A A 1970 *Int. J. Magn.* **1** 41
[3] Seeger M, Kaul S N, Kronmüller H and Reisser R 1995 *Phys. Rev.* B **51** 12 585
[4] Kaul S N 1988 *Phys. Rev.* B **38** 9178
[5] Kaul S N and Sambasiva Rao M 1991 *Phys. Rev.* B **43** 11 240
[6] Kaul S N and Sambasiva Rao M 1994 *J. Phys.: Condens. Matter* **6** 7403
    Sambasiva Rao M and Kaul S N 1995 *J. Magn. Magn. Mater.* **147** 149
[7] Babu P D and Kaul S N 1997 *J. Phys.: Condens. Matter* **9** 7189
[8] Semwal Anita and Kaul S N 2001 *Phys. Rev.* B **64** 014417-1
[9] Harris A B 1974 *J. Phys. C: Solid State Phys.* **7** 1671
[10] Lubensky T C 1975 *Phys. Rev.* B **11** 3573
[11] Khmel'nitskii D E 1976 *Sov. Phys.–JETP* **41** 981
     Khmel'nitskii D E 1975 *Zh. Eksp. Teor. Fiz.* **68** 1960
[12] Grinstein G and Luther A 1976 *Phys. Rev.* B **13** 1329
[13] Kaul S N 1985 *J. Magn. Magn. Mater.* **53** 5
[14] Fähnle M, Kellner W U and Kronmüller H 1987 *Phys. Rev.* B **35** 3640
     Kellner W U, Fähnle M, Kronmüller H and Kaul S N 1987 *Phys. Status Solidi* b **144** 397
[15] Hargraves P and Dunlap R A 1988 *J. Phys. F: Met. Phys.* **18** 533
[16] Kaul S N and Mohan Ch V 1994 *Phys. Rev.* B **50** 6157
[17] Kouvel J S and Comly J B 1971 *Critical Phenomena in Alloys, Magnets and Superconductors* ed R E Mills, E Ascher and R I Jaffee (New York: McGraw-Hill) p 437
[18] Jesser R, Bieber A and Kuentzler R 1983 *J. Physique* **44** 631
[19] Shen Y, Nakai I, Maruyama H and Yamada O 1985 *J. Phys. Soc. Japan* **54** 3915
[20] Seeger M and Kronmüller H 1989 *J. Magn. Magn. Mater.* **78** 393
[21] Boxberg O and Westerholt K 1994 *Phys. Rev.* B **50** 9331
[22] Seeger M, Kronmüller H and Blythe H J 1995 *J. Magn. Magn. Mater.* **139** 312
[23] Nelson J B and Riley D P 1945 *Proc. Phys. Soc.* **57** 160
     Taylor A and Sinclair H 1945 *Proc. Phys. Soc.* **57** 126
[24] Warren B E 1978 *X-Ray Diffraction* (London: Addison-Wesley)
[25] Grant W 1957 *J. Met.* **9** 865
[26] 1959 *International Tables for X-Ray Crystallography* vol 2 (Birmingham: Kynoch)
     1962 *International Tables for X-Ray Crystallography* vol 3 (Birmingham: Kynoch)
[27] 1967 *Metals Reference Book* 4th edn, vol 1 (New York: Plenum)
[28] Aoki K and Izumi O 1975 *Phys. Status Solidi* **32** 657 and references therein
[29] Semwal Anita and Kaul S N 1999 *Phys. Rev.* B **60** 12 799
[30] Aharony A and Fisher M E 1973 *Phys. Rev.* B **8** 3323
     Bruce A D and Aharony A 1974 *Phys. Rev.* B **10** 2078
     Bruce A D 1977 *J. Phys. C: Solid State Phys.* **10** 419
     Frey E and Schwabl F 1991 *Phys. Rev.* B **43** 833

[31] Larkin A I and Khmel'nitskii 1969 *Sov. Phys.–JETP* **29** 1123
Aharony A 1973 *Phys. Rev.* B **8** 3363
Bre'zin E and Zinn-Justin J 1976 *Phys. Rev.* B **42** 8261
Frey E and Schwabl F 1990 *Phys. Rev.* B **42** 8261
Ried K, Millev Y, Fähnle M and Kronmüller H 1995 *Phys. Rev.* B **51** 15 229
[32] Srinath S, Kaul S N and Kronmüller H 1999 *Phys. Rev.* B **59** 1145
Srinath S and Kaul S N 1999 *Phys. Rev.* B **60** 12 166
Griffin J A, Huster M and Folweiler R J 1980 *Phys. Rev.* B **22** 4370
[33] Wegner F J and Riedel E K 1973 *Phys. Rev.* B **7** 248
Bre'zin E 1975 *J. Physique* **36** L51
[34] Joyce G S 1966 *Phys. Rev.* **146** 349
[35] Sigfusson T I and Lonzarich G G 1982 *Phys. Scr.* **25** 720
[36] Semadeni F, Rosseli B, Böni P, Vorderwisch P and Chatterji T 2000 *Phys. Rev.* B **62** 1083
[37] Semwal Anita and Kaul S N 2002 *Pramana J. Phys.* at press
[38] Kaul S N 1983 *Phys. Rev.* B **27** 5761
[39] Wohlfarth E P 1978 *J. Magn. Magn. Mater.* **7** 113